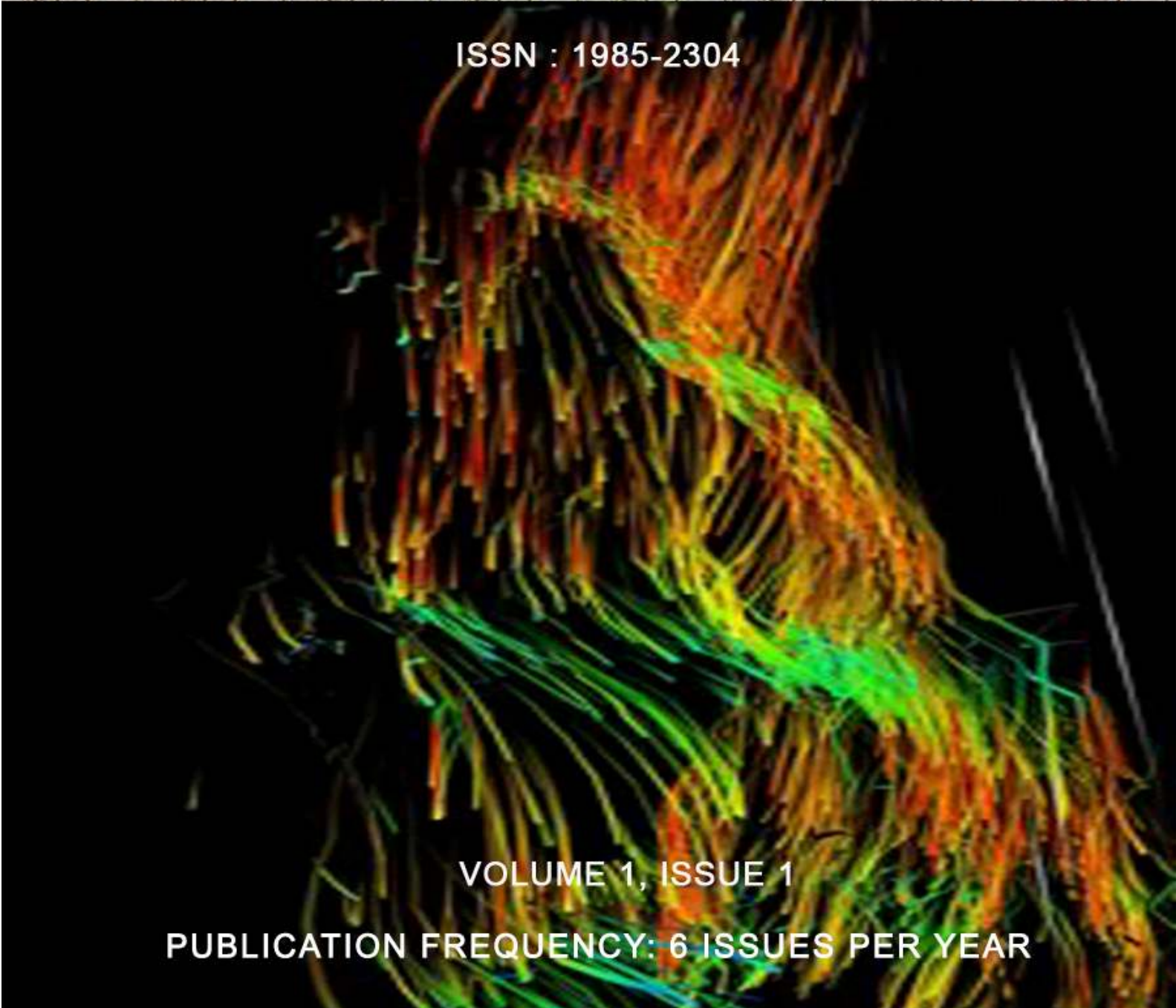


# International Journal of Image Processing (IJIP)



ISSN : 1985-2304



VOLUME 1, ISSUE 1

PUBLICATION FREQUENCY: 6 ISSUES PER YEAR

**Editor in Chief Professor Hu, Yu-Chen**

# **International Journal of Image Processing (IJIP)**

Book: 2007 Volume 1, Issue 1

Publishing Date: 30-06-2007

Proceedings

ISSN (Online): 1985-2304

This work is subjected to copyright. All rights are reserved whether the whole or part of the material is concerned, specifically the rights of translation, reprinting, re-use of illustrations, recitation, broadcasting, reproduction on microfilms or in any other way, and storage in data banks. Duplication of this publication of parts thereof is permitted only under the provision of the copyright law 1965, in its current version, and permission of use must always be obtained from CSC Publishers. Violations are liable to prosecution under the copyright law.

IJIP Journal is a part of CSC Publishers

<http://www.cscjournals.org>

© IJIP Journal

Published in Malaysia

Typesetting: Camera-ready by author, data conversion by CSC Publishing Services – CSC Journals, Malaysia

**CSC Publishers**

# Table of Contents

Volume 1, Issue 1, May/June 2007.

## Pages

- 1 - 16      Correction of Inhomogeneous MR Images Using Multiscale Retinex  
**Wen-Hung Chao, Chien-Wen Cho, Yen-Yu Shih, You-Yin Chen, Chen Chang.**

## Correction of Inhomogeneous MR Images Using Multiscale Retinex

Wen-Hung Chao<sup>1,2</sup>

[wenhong@mail.ypu.edu.tw](mailto:wenhong@mail.ypu.edu.tw)

<sup>1</sup> Department of Biomedical Engineering, Yuanpei University, No.306, Yuanpei St., Hsinchu City, Taiwan 300, R.O.C.

Chien-Wen Cho<sup>2</sup>

[gustafcho@gmail.com](mailto:gustafcho@gmail.com)

<sup>2</sup>Department of Electrical and Control Engineering, National Chiao Tung University, No. 1001, Ta-Hsueh Rd., Hsinchu City, Taiwan 300, R.O.C.

Yen-Yu Shih<sup>3</sup>

[f93548021@ntu.edu.tw](mailto:f93548021@ntu.edu.tw)

<sup>3</sup>Institute of Biomedical Engineering, National Taiwan University, No.1, Sec.1, Jen-Ai Rd., Taipei City, Taiwan, 100, R.O.C.

You-Yin Chen<sup>2,\*</sup>

[irradiance@so-net.net.tw](mailto:irradiance@so-net.net.tw)

<sup>2</sup>Department of Electrical and Control Engineering, National Chiao Tung University, No. 1001, Ta-Hsueh Rd., Hsinchu City, Taiwan 300, R.O.C.

\*Corresponding author: Tel: +886-3-571-2121 ext 54427; Fax: +886-3- 612-5059.

Chen Chang<sup>4</sup>

[bmcchen@ibms.sinica.edu.tw](mailto:bmcchen@ibms.sinica.edu.tw)

<sup>4</sup>Functional and Micro-Magnetic Resonance Imaging Center, Institute of Biomedical Sciences, Academic Sinica, No.128, Sec. 2., Yen-Chiu-Yuan Rd, Taipei City, Taiwan 115, R.O.C.

---

### Abstract

A new method for enhancing the contrast of magnetic resonance images (MRI) by retinex algorithm is proposed. It can correct the blurrings in deep anatomical structures and inhomogeneity of MRI. Multiscale retinex (MSR) employed SSR with different weightings to correct inhomogeneities and enhance the contrast of MR images. The method was assessed by applying it to phantom and animal images acquired on MRI scanner systems. Its performance was also compared with other methods based on two indices: (1) the peak signal-to-noise ratio (PSNR) and (2) the contrast-to-noise ratio (CNR). Two indices, including PSNR and CNR, were used to evaluate the performance of correction of inhomogeneity in MR images. The PSNR/CNR of a phantom and animal images were 11.8648 dB/2.0922 and 11.7580 dB/2.1157, respectively, which were higher or very close to the results of wavelet algorithm. The retinex algorithm successfully corrected a nonuniform grayscale, enhanced contrast, corrected inhomogeneity, and clarified the deep brain structures of MR images captured by surface coils and outperformed histogram equalization, local histogram equalization, and a wavelet-based algorithm, and hence may be a valuable method in MR image processing.

**Keywords:** Magnetic resonance imaging, Surface coils, Single-scale Retinex, multiscale retinex, Peak signal-to-noise ratio, Contrast-to-noise ratio.

---

## 1. INTRODUCTION

Magnetic resonance imaging (MRI) has been used to diagnose various diseases over the past two decades and represented an important diagnostic technique in medicine [2] for the effective and noninvasive detection of objects such as cancers and tumors. Several techniques have been recently developed to improve the detection and diagnosis capabilities [5], including eliminating artifacts and enhancing the contrast of MR images [6, 7]. Zoroofi et. al [7] used a postprocessing technique to reduce MRI body motion artifacts due to the presence of an object on the imaging plane. They proposed a reconstruction algorithm, based on a superposition bilinear interpolation algorithm, reducing such artifacts with a minimum-energy method to estimate the unknown parameters of body motion. Results showed feasibility in clinical application. Sled et al [8] demonstrated the efficacy of an automatic nonparametric method in correcting intensity nonuniformities using both real and simulated MR data. Ahn et al [9] proposed a method of local adaptive template filtering for enhancing the signal-to-noise ratio (SNR) in MRI without reducing the resolution. Moreover, Styner et al [10] showed that a parametric bias-field correction method could correct bias distortions that are much larger than the image contrast. Likar et al [11] proposed a model-based correction method to adjust inhomogeneity in the intensity of an MR image. They applied an inverse image-degradation model where parameters were optimized by minimizing the information content of simulated and real MR data. Lin et al [12] used a wavelet-based algorithm to approximate surface-coil sensitivity profiles. They corrected image intensity in homogeneities acquired by surface coils, and used a parallel MRI method to verify the spatial sensitivity profile of surface coils from the images captured without using a body coil. It has also been shown [13, 14] that contrast enhancement can be used to improve the quality of MR images. Several MRI-related techniques have been suggested to facilitate more accurate clinical diagnoses [1, 2, 15]. Among them, surface coils were used to enhance the SNR and improve the resolution [15]. A surface coil consisted of conductive loops that transmit radiofrequency (RF) energy can also be used as receivers. They exhibited maximal sensitivity in localizing surface structures and facilitate faster MRI scanning [15–18]. The use of stronger gradients increased the spatial resolution but reduced the sensitivity. Nevertheless, the location of surface coils must be controlled to increase sensitivity. Image quality can be improved by reducing the thermal noise generated outside the region of sensitivity, eliminating artifacts due to body movements and respiration, and using steep imaging gradients. Another obvious disadvantage of planar surface coils was that the low signal level made it difficult to image deep brain structures, resulting in a large dynamic range of signal intensities in MR images. Dynamic-range compression has been used to solve this problem [14, 15], with views of larger regions being captured by a phased array of surface coils [19]. Phased-array surface coils can be implemented by switching among multiple surface-coil receivers. This improved the SNR and increased the clinical applications, but the problem of signal loss in deep brain structures remained. Therefore, an optimum contrast-enhancement algorithm would be helpful to improve the quality of MR images acquired by surface coils.

Stretching the pixel dynamic range of certain objects in an image is a widely adopted approach for enhancing the contrast [20]. The image contrast-enhancement techniques can be divided into two types: global and local histogram enhancement [21, 22]. The (global) histogram equalization technique improved the uniformity of the intensity distribution of an image [21, 22] by equalizing the number of pixels at each gray level. The disadvantage of this method is that it is not effective in improving poor localized contrasts [23]. Local histogram enhancement [22, 24] used an equalization method to improve the detailed histogram distribution within small regions of an image, and also preserved the gray-level values of the image. The obtained histogram is updated in neighboring regions at each iteration, then local histogram equalization is applied. However, the visual perception quality of a processed image is subjective, and it is known that both global and local histogram equalization do not result in the best contrast enhancement [22–27].

For image processing, the presence of the nonuniformity of an MR image caused by the inhomogeneity of the magnetic intensity is very similar to that of a normal image resulted from bad illumination sources and environmental conditions. To address the nonuniformity problem of an image, Land [28], inspired by the psychological knowledge about the brain's processing of image information from retinas, developed a concept named retinex as a model for describing the color constancy in human visual perception. His idea is that the perception of human is not completely

defined by the spectral character of the light reaching the eye from scenes. It includes the processing of spatial-dependant color and intensity information of the retina of an eye, which can be realized by the computation of dynamic-range compression and color rendition [29–32]. Moreover, Jobson et al [33] found in his study that the selection the parameters of surrounding function can greatly affect the performance of the retinex. He then balanced the dynamic compression and color rendition by using multi-scale retinex (MSR). Although hardware techniques can be utilized to correct the image inhomogeneity and to enhance image contrast, they are costly and inflexible. Hence, it is promising to develop easy and low-cost software-based techniques to address the inhomogeneity problem in MR images. In this study, we introduced a software-based retinex algorithm for contrast enhancement and dynamic-range compression that improve image quality by decreasing image inhomogeneity.

## 2. MATERIALS AND METHODS

### 2.1 Retinex Algorithm

In general, the human visual system is better than machines when processing images. Observed images of a real scene are processed based on brightness variations. The images captured by machines are easily affected by environmental lightening conditions, which tends to reduce its dynamic range. On the contrary, the human visual system can automatically compensate the image information by psychological mechanism of color constancy. Color constancy, an approximation process of human perception system, makes the perceived color of a scene or objects remain relatively constant even with varying illumination conditions. Land [28] proposed a concept of the retinex, formed from "retina" and "cortex", suggesting that both the eye and the brain are involved, to explain the color constancy processing of human visual systems. After the human visual system obtain the approximate of the illuminating light, the illumination is then discounted such that the "true color" or reflectance can be determined. More details about subject color constancy can be found in [1, 3].

Hurlbert and Poggio [31] and Hurlbert [32] applied the retinex properties and luminosity principles to derive a general mathematical function. Differences arose when images from various center/surround functions in three scales of gray-level variations were shown. Hurlbert [31–32] applied a center/surround function to solve the brightness problem, using the learning mechanism of neural networks and a general solution to evaluate the relative brightness in arbitrary environments.

Although Jobson et al proposed a single-scale retinex (SSR) algorithm that could support different dynamic-range compressions [33, 34], the multi-scale retinex (MSR) can better approximates human visual processing, verified by experiments [33–36], by transforming recorded images into a rendering which is much closer to the human perception of the original scene.

### 2.2 Single-Scale Retinex

The basics of an SSR [28] were briefly described as follows. A logarithmic photoreceptor function that approximates the vision system was applied, based on a center/surround organization [28, 34]. The SSR was given by

$$R_i(x, y) = \log I_i(x, y) - \log[(I_i(x, y) * F(x, y))], \quad (1)$$

where  $R_i(x, y)$  was the retinex output,  $I_i(x, y)$  was the image distribution in the  $i$ th spectral band, and "\*" represented the convolution operator. In addition,  $F(x, y)$  was represented as

$$\iint F(x, y) dx dy = 1, \quad (2)$$

which was the normalized surround function. The purpose of the logarithmic manipulation was to transform a ratio at the pixel level to a mean value for a larger region. We selected MR images for our implementation with this form in Eq. (5) proposed by Land [28].

This operation was applied to each spectral band to improve the luminosity, as suggested by Land [28]. It was independent from the spectral distribution of a single-source illumination since

$$I_i(x, y) = S_i(x, y)r_i(x, y), \quad (3)$$

where  $S_i(x, y)$  was the spatial distribution on an illumination source, and  $r_i(x, y)$  was the

reflectance distribution in an image, so

$$R_i(x, y) = \log \frac{S_i(x, y)r_i(x, y)}{\overline{S}_i(x, y)\overline{r}_i(x, y)}, \quad (4)$$

$$S_i(x, y) \approx \overline{S}_i(x, y), \quad (5)$$

where  $\overline{S}$  represented the spatially weighted average value, as long as

$$R_i(x, y) \approx \log \frac{r_i(x, y)}{\overline{r}_i(x, y)}. \quad (6)$$

This approximate equation was the reflectance ratio, and was equivalent to illumination variations in many cases.

### 2.3 The Surround Function

Several types of surround function were implemented. First, an inverse-square spatial surround function proposed by Land [28] was formed as

$$F(x, y) = 1/r^2, \quad (7)$$

where

$$r = \sqrt{x^2 + y^2} \quad (8)$$

could be changed to another surround function as

$$F(x, y) = \frac{1}{1 + (r^2/c_1^2)}, \quad (9)$$

where  $c_1$  was a space constant.

Moore et al [29, 30] used a surround function on an exponential function with the absolute value  $r$  as

$$F(x, y) = e^{-r/c_2} \quad (10)$$

to approximate the spatial response, where  $c_2$  was a space constant.

Hurlbert and Poggio [31] and Hurlbert [32] used the Gaussian surround function

$$F(x, y) = Ke^{-r^2/c_3^2} \quad (11)$$

to reconcile natural and human vision, where  $c_3$  was a space constant. For a given space constant, the inverse-square surround function accounted for a greater response from the neighboring pixels than the exponential and Gaussian functions. The spatial response of the exponential surround function was larger than that of the Gaussian function at distant pixels. Therefore, the inverse-square surround function was more commonly used in global dynamic-range compression, and the Gaussian surround function was generally used in regional dynamic-range compression [33].

The exponential and Gaussian surround functions were able to produce good dynamic-range compression over neighboring pixels [29, 32, 33]. From the proposed surround functions [29–32], the Gaussian surround function exhibited good performance over a wider range of space constants, so it was used to enhance contrasts and to solve the inhomogeneity of MR images in the present study.

### 2.4 Adjustment of Single-Scale Retinex Output

The final process output was not obvious from the center/surround retinex proposed by Land [28]. Moore et al [29] also offered an automatic gain and offset operation, in which the triplet retinex outputs were regulated by the absolute maximum and minimum values of all scales in a scene. In this study, a constant gain and offset technique (as shown in Fig. 1) was used to select the best rendition.

Fig. 1 described how to choose the transferred output interval of both the highest- and lowest-scale rendition scene for each SSR. The offset value can be directly determined by the lower

bound. Furthermore, the gain can be computed according to the range between the upper and lower bounds. The selection of a larger upper bound led to minor contrast improvement but prevents heavy distortion caused by truncation. The lower bound functions in a similar way as explained previously. Adjustments to the gain and offset result in the retinex outputs caused little information lost, and the constant gain and offset of retinex was independent of the image content. We evaluated the effects of variations in the histogram characteristics in a gray-level scene. The gain and offset were constant between images in accordance with the original algorithm proposed by Land [28], and also demonstrated that it can be applied as a common manipulation to most types of images.

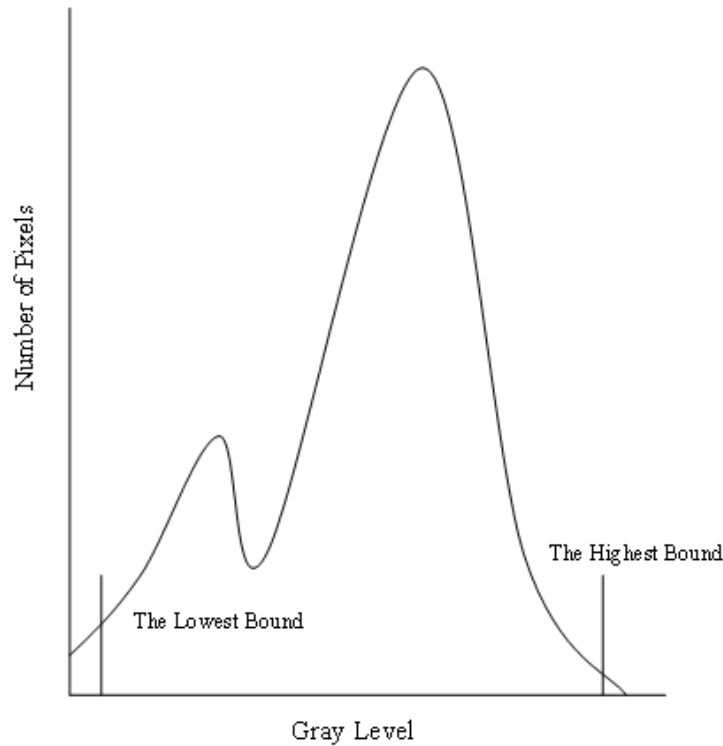


**FIGURE 1:** A histogram distribution plot that illustrated the gain and offset values of an MR image, which underwent the single-scale retinex (SSR) to enhance its contrast.

## 2.5 Multiscale Retinex

It was our intention to select the best value of scale factor  $c$  in the surround function  $F(x, y)$  based on the dynamic-range compression and brightness rendition for every SSR. We also intended to maximize the optimization of the dynamic-range compression and brightness rendition. MSR was a good method for summing a weighted SSR according to

$$R_{MSRi} = \sum_{n=1}^N \omega_n R_{ni} , \quad (12)$$

where  $N$  represented a scaling parameter,  $R_{ni}$  represented the  $i$ th component of the  $n$ th scale,  $R_{MSRi}$  was the  $n$ th spectral component of the MSR output, and  $\omega_n$  represented the multiplication weight for the  $n$ th scale. The differences between  $R(x, y)$  and  $R_n(x, y)$  resulted in surround

function  $F_n(x, y)$  became

$$F_n(x, y) = Ke^{-r^2/c_n^2}. \quad (13)$$

MSR combined various SSR weightings [33, 34], selecting the number of scales used for the application and evaluating the number of scales that can be merged. Important issues to be concerned were the number of scales and scaling values in the surround function, and the weights in the MSR. MSR was implemented by a series of MR images, based on a trade-off between dynamic-range compression and brightness rendition. Also, we needed to choose the best weights in order to obtain suitable dynamic-range compression at the boundary between light and dark parts of the image, and to maximize the brightness rendition over the entire image. We verified the MSR performances on visual rendition with a series of MR images scanned by MR systems. Furthermore, we compared the efficacy of the MSR technique in enhancing the contrast of these MR images with other image processing techniques.

An algorithm for MSR as applied to human vision has been described in past literature [33, 34]. The MSR worked by compensating for lighting variations to approximate the human perception of a real scene. There were two methods to achieve this: (1) compare the psychophysical mechanisms between the human visual perceptions of a real scene and a captured image, and (2) compare the captured image with the measured reflectance values of the real scene.

To summarize, our method involved combining specific features of MSR with processes of SSR, in which the center/surround operation was a Gaussian function. A narrow Gaussian distribution was used for the neighboring areas of a pixel (which was regarded as the center). Space constants for Gaussian functions with scales of 15, 80, and 250 pixels in the surrounding area, as proposed by Jobson et al [33, 34], were adopted in this study. The logarithm was then applied after surround function processing (i.e., two-dimensional spatial convolution). Next, appropriate gain and offset values were determined according to the retinex output and the characteristics of the histogram. These values were constant for all the images. This procedure yielded the MSR function.

## 2.6 Phantom and Animal Magnetic Resonance Imaging

All experiments were performed at the NMR Center, Institute of Biomedical Sciences, Academia Sinica. They were carried out in accordance with the guidelines established by the Academia Sinica Institutional Animal Care and Utilization Committee.

A single adult male Wistar rat weighing 275 g (National Laboratory Animal Center, Taiwan) was anesthetized using 2 % isoflurane and positioned on a stereotaxic holder. The body temperature of the animal was maintained using a warm-water circulation system.

For MR experiments, images were captured on a Bruker BIOSPEC BMT 47/40 spectrometer (Bruker GmbH, Ettlingen, Germany), operating at 4.7 Tesla (200 MHz), equipped with an actively shielded gradient system (0 ~ 5.9 G/cm in 500 ms). A 20-cm volume coil was used as the RF transmitter, and a 2-cm linear surface coil and the above volume coil were used separately as the receiver. Coronal T2-weighted images of the phantom – comprising a 50-ml plastic centrifuge tube filled with water and an acrylic rod – and the rat brain were acquired using RARE sequences with a repetition time of 4000 ms, an echo time of 80 ms, a field of view of 3 cm, a slice thickness of 1.5 mm, 2 repetitions, and an acquisition matrix of 256 × 256 pixels.

## 2.7 Peak Signal-to-Noise Ratio and Contrast-to-Noise Ratio Analysis

The PSNR [37] and contrast-to-noise ratio (CNR) were commonly used performance indices in image processing [9, 38]. The PSNR was given by

$$PSNR = 20 \log \frac{I_{peak}}{\sqrt{\sum_{k,l} \{y(k,l) - m(k,l)\}^2 / (K \cdot L)}}, \quad (14)$$

where  $y(k, l)$  and  $m(k, l)$  were the enhanced and original images of size  $K$  and  $L$  respectively, and  $I_{peak}$  was the maximum magnitude of images [37]. The CNR was given by

$$CNR = \frac{E[P_{jk}^d] - E[P_{jk}^u]}{\sqrt{\frac{Var(P_{jk}^d) + Var(P_{jk}^u)}{2}}}, \quad (15)$$

where  $P_{jk}^d$  and  $P_{jk}^u$  were the gray levels,  $E[P_{jk}^d]$  and  $E[P_{jk}^u]$  were the means, and  $Var(P_{jk}^d)$  and  $Var(P_{jk}^u)$  were the variances of the  $(j, k)$ th pixel in the enhanced and original images respectively [9, 38].

### 3. RESULTS

#### 3.1 Phantom Image

The performance of our retinex algorithm was assessed by determining the parameters for a test series of MR images of the phantom, with dimensions of  $256 \times 256$  pixels and 16-bit quantization. The dynamic-range compression and brightness constancy were determined in the MR images of the test series, based on postprocessing by the retinex method.

Fig. 2 showed the results of using SSR and MSR to correct for the inhomogeneity of an MR image of the phantom. The original MR image was shown in Fig. 2(a), which exhibited inhomogeneity, nonuniformity, low brightness, and a large dynamic range. SSR with a scale of every 10 pixels between 0 and 255 was used to analyze the series of phantom images. SSR with a scale of 15 pixels was also applied in this test. Fig. 2(b), (c), and (d) illustrated the successful reductions in intensity inhomogeneity of the phantom images using SSR with scales of 15, 80, and 250 pixels respectively. The images in Fig. 2(b), (c), and (d) showed dynamic-range compressions and brightness were large, moderate, and small, respectively, which indicated the dynamic-range compression increased when the SSR scale decreased. Fig. 2(e) showed the image obtained from MSR by combining three scales of SSR weightings ( $\omega_n = 1/3$ ,  $n = 1, 2$ , and 3), where the three scales of SSR were 15, 80, and 250 pixels as used by Jobson et al [33, 34]. The images obtained from the retinex algorithms were of higher quality than the original phantom image. Also, Fig. 2(f) showed an MR image captured by a volume coil as a receiver with the same MR imaging procedures and parameters. Comparison of Fig. 2(e) and (f) revealed that MSR successfully corrected the original MR phantom image.

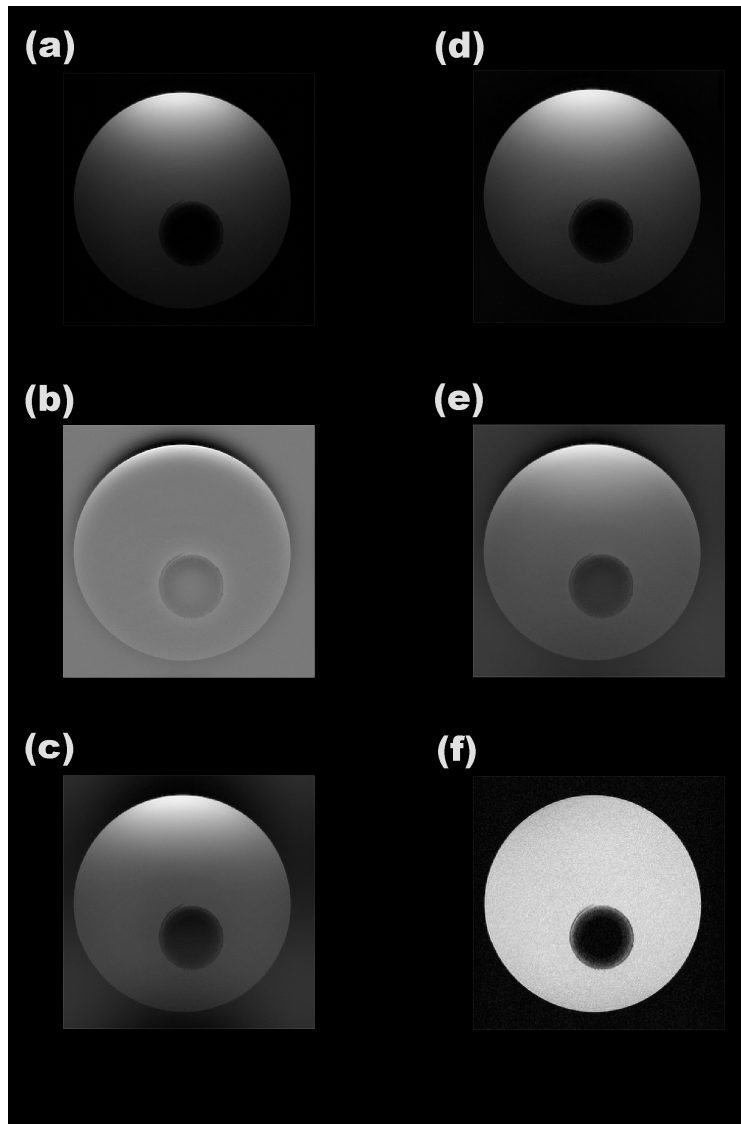


**FIGURE 2:** Corrected MR images of a phantom demonstrating the performance of retinex. (a) The original MR image. (b) Image obtained from SSR with scale of 15 pixels. (c) Image obtained from SSR with scale of 80 pixels. (d) Image obtained from SSR with scale of 250 pixels. (e) Image obtained from MSR with three combined scales of SSR weightings ( $\omega_n = 1/3$ ,  $n = 1, 2$ , and  $3$ ). (f) MR image captured by a volume coil.

### 3.2 Animal Image

In Fig. 3, results of applying SSR and MSR to adjust a rat brain MR image were shown. Fig. 3(a) showed the original MR image, which was one of 28 coronal brain slices. Fig. 3(b), (c), and (e) showed the images obtained from SSR with scales of 15, 80, and 250 pixels respectively, with dynamic-range compressions that are large, moderate, and small; and brightness variations that are small, moderate, and large respectively. The images obtained from retinex demonstrated better visual rendition than that of the original MR image in Fig. 3(a). The background of the original brain MR image was blurred, and its brightness contrast and dynamic range were poor. Fig. 3(d) was the image obtained from MSR, displaying its strength of combining small, moderate, and large scales of SSR with the same weightings of  $\omega_n = 1/3$  ( $n = 1, 2$ , and  $3$ ). Fig. 3(f) showed an MR image captured by a volume coil with the same MR imaging procedure, it had better homogeneity than the image obtained by surface coils, yet the resolution was lower. Fig. 3(g) was enlarged ( $\times 5$ ) from dotted-line block of the original image in Fig. 3(a), showing the deep brain

structure subimage, the details in the medial forebrain bundle (MFB) and mammillothalamic tract (MT) regions were not clear and inhomogeneous.

Fig. 3(h) showed the MR image enlarged ( $\times 5$ ) from dotted-line block of Fig. 3(d) from MSR, regions (MFB and MT) circled with dotted-curve demonstrated better homogeneity and clarity. Fig. 3(h) exhibited clearer deep anatomical structures from MSR than Fig. 3(g) from original image.

The MSR clearly improved the quality, relative to that of the original MR image. Comparing among the original MR image, the image captured by a volume coil and the image obtained from the retinex algorithm revealed that the last method showed the best performance in terms of brightness, dynamic-range compression, and overall visual rendition.

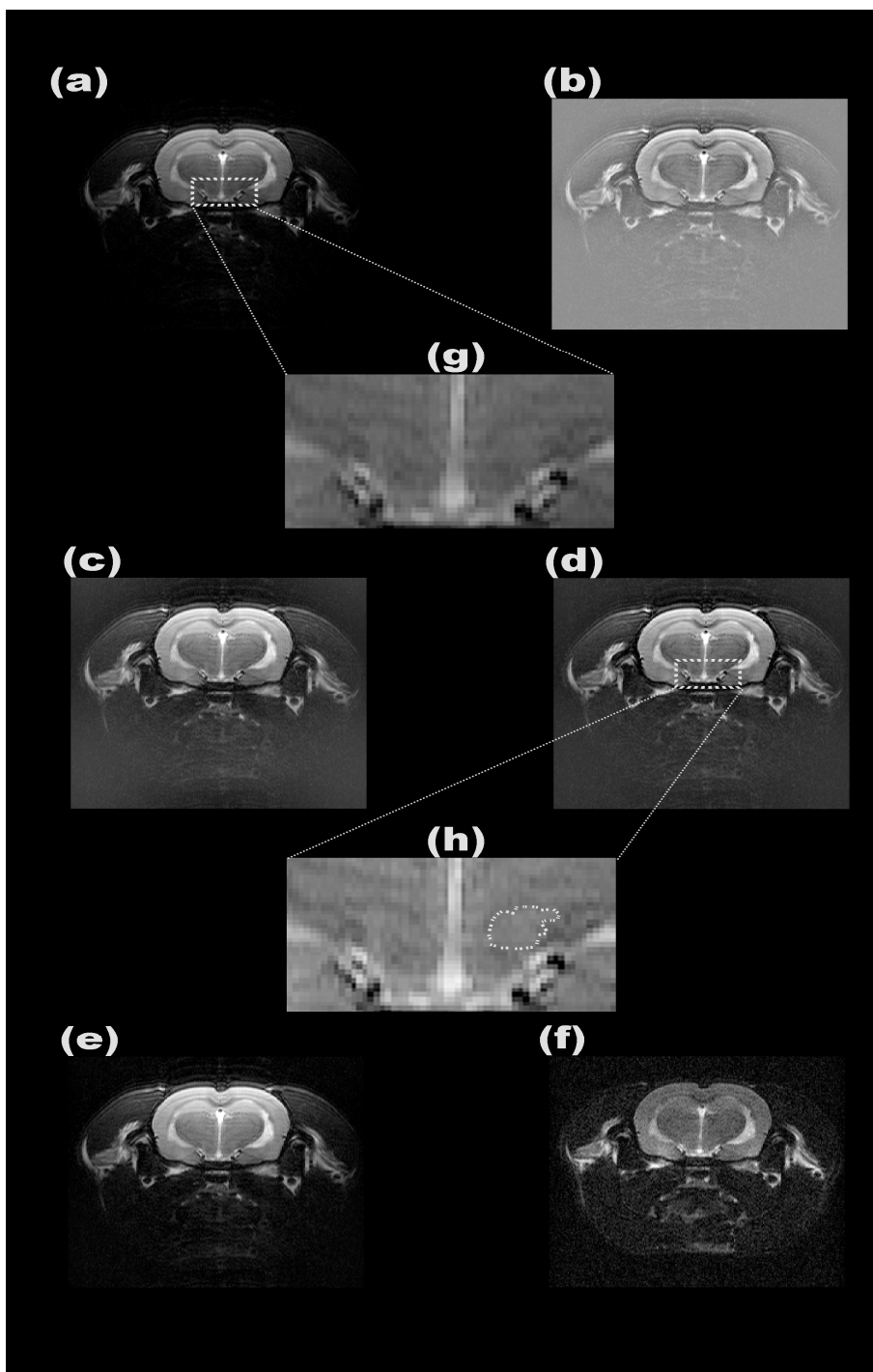


**FIGURE 3:** Performance of the retinex was demonstrated with adjusted MR images of a coronal section of the rat brain. (a) The original MR image. (b) Image obtained from SSR with scale of 15 pixels. (c) Image obtained from SSR with scale of 80 pixels. (d) Image obtained from MSR with three combined scales of SSR weightings ( $\omega_n = 1/3$ ,  $n = 1, 2$ , and  $3$ ). (e) Image obtained from SSR with scale of 250 pixels. (f) MR image captured by a volume coil. (g) A 500% enlargement from the dotted-line block area in (a). The enlargement exhibits areas of tissue inhomogeneity within the deep brain structures. (h) The enlarged medical forebrain bundle (MFB), from dotted-line block of (d). The MFB was more clearly differentiated from other structures and the homogeneity of the circled region can be guaranteed.

### 3.3 Comparisons of Histogram Equalization, Local Histogram Equalization, and a Wavelet-Based Algorithm with Multiscale Retinex

The effectiveness of the retinex algorithm was compared with a phantom image captured by MR imaging systems, using histogram equalization, local histogram equalization, and a wavelet-based algorithm.

In Fig. 4(a), the image was obtained with histogram equalization, and Fig. 4(b) showed the image obtained from local histogram equalization with a local region of  $128 \times 128$  pixels. Both techniques resulted in blurred edges and poor contrast. A large amount of noise was still present in Fig. 4(a) and (b), with the performance of local histogram equalization being worse than that of histogram equalization. Fig. 4(c) showed the image processed by the wavelet-based algorithm [12, 13], indicating the presence of some noise. In Fig. 4(d) and (e), the images were obtained from MSR with combined 15-pixel small-scale SSR weightings of  $\omega_1 = 3/5$  and  $4/6$ ; 80-pixel moderate-scale SSR weightings of  $\omega_2 = 1/5$  and  $1/6$ ; and 250-pixel large-scale SSR weightings of  $\omega_3 = 1/5$  and  $1/6$  respectively. Fig. 4 (f) showed the image obtained from MSR with combined 10-pixel small-scale SSR weightings of  $\omega_1 = 3/5$ ; 60-pixel moderate-scale SSR weightings of  $\omega_2 = 1/5$ ; and 220-pixel large-scale SSR weightings of  $\omega_3 = 1/5$ . All phantom figures in Fig. 4 displayed clear deep structures and edges. The MSR algorithm exhibited better visual rendition than histogram equalization, local histogram equalization, and the wavelet-based algorithm. The performance of MSR was also compared with those of histogram equalization, local histogram equalization, and the wavelet-based algorithm on an MR image of rat brain.

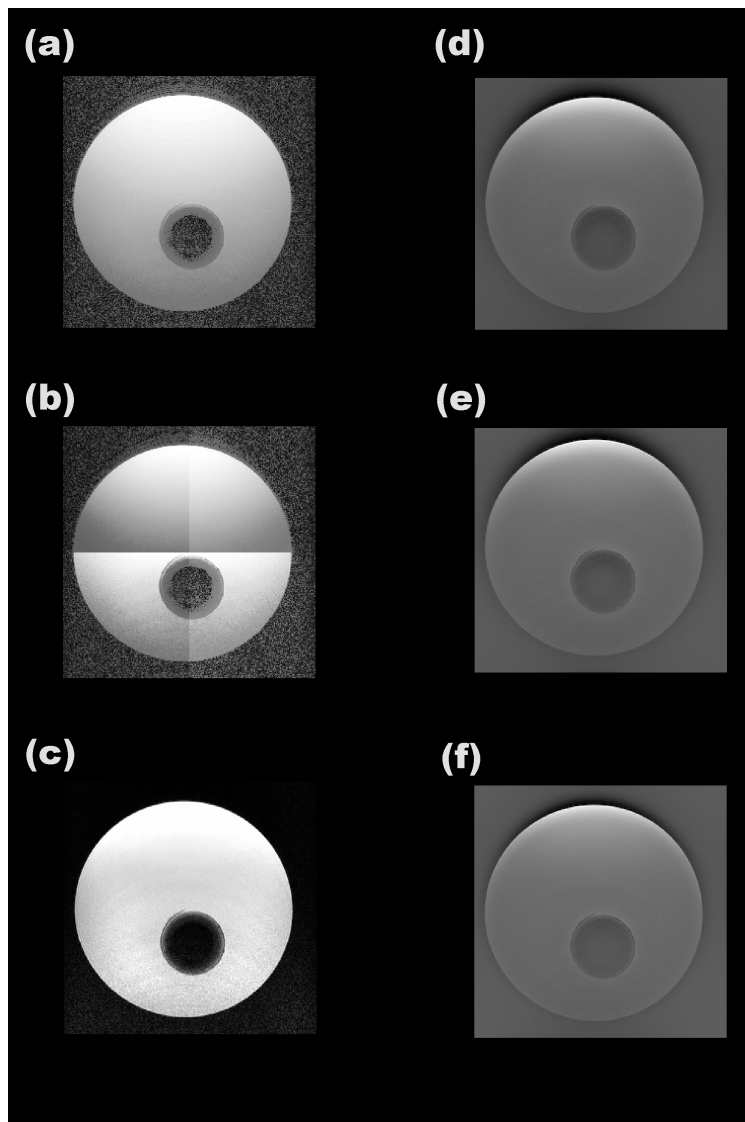


**FIGURE 4:** Corrected MR images of a phantom, obtained via four methods. (a) MR image obtained from histogram equalization. (b) MR image obtained from local histogram equalization. (c) MR image obtained with the wavelet-based algorithm. (d) and (e) MR images from MSR with 15-pixel, 80-pixel, and 250-pixel;  $\omega_1 = 3/5$  and  $4/6$ ,  $\omega_2 = 1/5$  and  $1/6$ , and  $\omega_3 = 1/5$  and  $1/6$  respectively. (f) MR image from MSR with 10-pixel, 60-pixel, and 220-pixel;  $\omega_1 = 3/5$ ,  $\omega_2 = 1/5$ , and  $\omega_3 = 1/5$  respectively.

Fig. 5(a) showed the corrected image obtained with histogram equalization, and Fig. 5(b) showed the image obtained from local histogram equalization with a local region of  $128 \times 128$  pixels. Both techniques resulted in blurred edges and poor contrast. A large amount of noise was still present in Fig. 5(a) and (b), with the performance of local histogram equalization being worse than that of histogram equalization. In Fig. 5(c), the image was processed by the wavelet-based algorithm [12, 13], resulting in many artifacts. Fig. 5(d) showed the image corrected by MRS with configuration of 15-pixel small-scale SSR weightings of  $\omega_1 = 2/4$  (high brightness), 80-pixel moderate-scale SSR weightings of  $\omega_2 = 1/4$  (moderate brightness), and 250-pixel large-scale SSR weightings of  $\omega_3 = 1/4$  (low brightness). Fig. 5(e) showed the image corrected by MRS with configuration of 10-pixel small-scale SSR weightings of  $\omega_1 = 1/3$  (high brightness), 60-pixel moderate-scale SSR weightings of  $\omega_2 = 1/3$  (moderate brightness), and 220-pixel large-scale SSR weightings of  $\omega_3 = 1/3$  (low brightness). Fig. 5(f) showed the image corrected by MRS with configuration of 10-pixel small-scale SSR weightings of  $\omega_1 = 2/6$  (high brightness), 60-pixel moderate-scale SSR weightings of  $\omega_2 = 3/6$  (moderate brightness), and 220-pixel large-scale SSR weightings of  $\omega_3 =$

1/6 (low brightness). The dynamic compression, brightness variation, and overall rendition were better for MSR that combined three scales of SSR weightings than those for histogram equalization, local histogram equalization, or the wavelet-based algorithm alone. All rat brain figures in Fig. 5 displayed clear deep anatomy structures and edges.

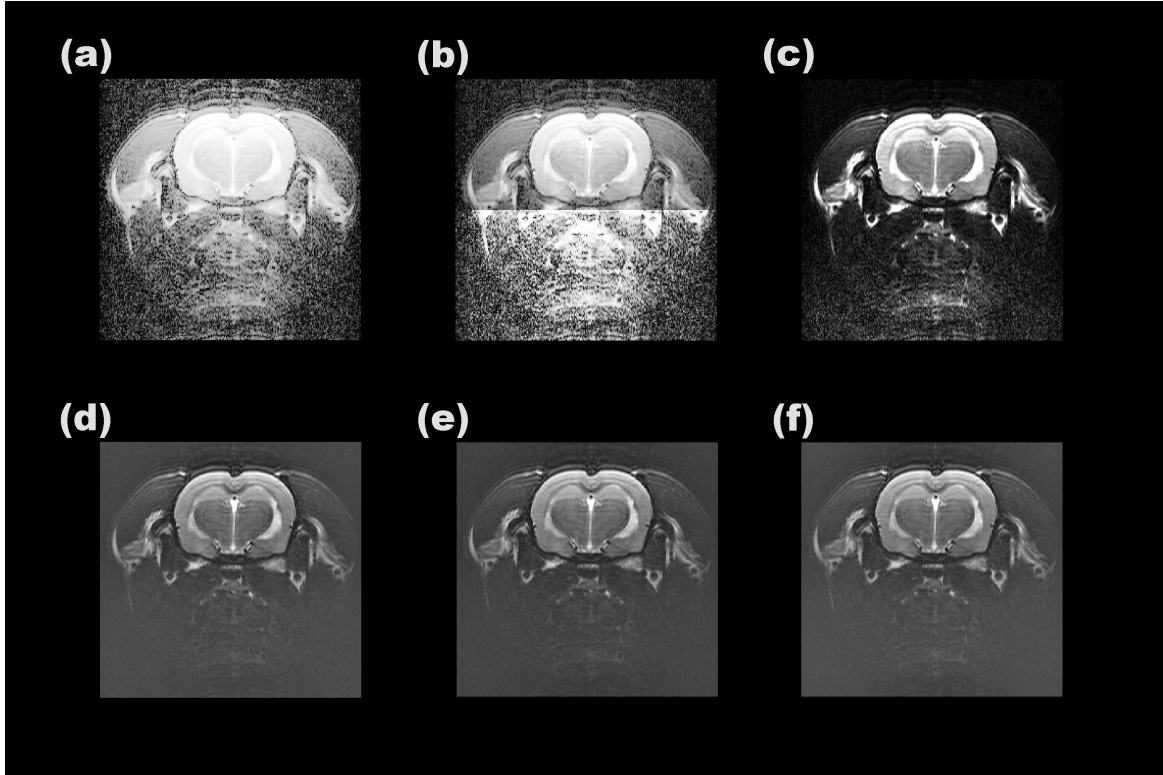


**FIGURE 5:** Corrected MR images of a rat brain obtained from four algorithms. (a) MR image obtained from histogram equalization. (b) MR image obtained from local histogram equalization. (c) MR image obtained from the wavelet-based algorithm. (d) MR image obtained from MSR, with 15-pixel, 80-pixel, and 250-pixel;  $\omega_1 = 2/4$ ,  $\omega_2 = 1/4$ , and  $\omega_3 = 1/4$  respectively. (e) and (f) MR images obtained from MSR with 10-pixel, 60-pixel, and 220-pixel;  $\omega_1 = 1/3$  and  $2/6$ ,  $\omega_2 = 1/3$  and  $3/6$ , and  $\omega_3 = 1/3$  and  $1/6$  respectively.

### 3.4 Results of Peak Signal-to-Noise Ratio and Contrast-to-Noise Ratio Analysis

Obtaining MR images of the highest possible clarity is crucial to effective structural brain imaging. The quality of images obtained from histogram equalization, local histogram equalization, the wavelet-based algorithm, and retinex can be quantified using appropriate indices. The values of PSNR and CNR for the phantom images obtained in the present study with the four correction methods were listed in Table 1, where higher values indicate images of higher quality. As shown on the table, the use of SSR increased PSNR but decreased CNR. In Tables 1 and 2, MSR showed combined small-, moderate-, and large-scale weightings of 15, 80, and 250 pixels respectively, and MSR<sub>2</sub> indicated combined small-, moderate-, and large-scale weightings of 10, 60, and 220 pixels respectively. In Table 1, MSR with  $\omega_1 = 3/5$ ,  $\omega_2 = 1/5$ , and  $\omega_3 = 1/5$ ; MSR with  $\omega_1 = 4/6$ ,  $\omega_2 = 1/6$ , and  $\omega_3 = 1/6$ ; and MSR<sub>2</sub> with  $\omega_1 = 2/4$ ,  $\omega_2 = 1/4$ , and  $\omega_3 = 1/4$ , and MSR<sub>2</sub> with  $\omega_1 = 3/5$ ,  $\omega_2 = 1/5$ , and  $\omega_3 = 1/5$  resulted in higher values of PSNR and CNR than histogram equalization, local histogram equalization, and the wavelet-based algorithm.

The values of PSNR and CNR for animal images were listed in Table 2. Whilst histogram equalization and local histogram equalization resulted in high CNR values, the low PSNR values resulted in many noise artifacts. The wavelet-based algorithm resulted in some noise, as indicated by the lower CNR value. MSR with  $\omega_1 = 1/3$ ,  $\omega_2 = 1/3$ , and  $\omega_3 = 1/3$ ; MSR with  $\omega_1 = 2/4$ ,  $\omega_2 = 1/4$ , and  $\omega_3 = 1/4$ ; MSR with  $\omega_1 = 1/4$ ,  $\omega_2 = 2/4$ , and  $\omega_3 = 1/4$ ; MSR with  $\omega_1 = 1/5$ ,  $\omega_2 = 3/5$ , and  $\omega_3 =$

1/5; MSR<sub>2</sub> with  $\omega_1 = 1/3$ ,  $\omega_2 = 1/3$ , and  $\omega_3 = 1/3$ ; MSR<sub>2</sub> with  $\omega_1 = 1/4$ ,  $\omega_2 = 2/4$ , and  $\omega_3 = 1/4$ ; and MSR<sub>2</sub> with  $\omega_1 = 2/6$ ,  $\omega_2 = 3/6$ , and  $\omega_3 = 1/6$  resulted in higher values of PSNR and CNR than histogram equalization, local histogram equalization, and the wavelet-based algorithm.

Algorithm	PSNR (dB)	CNR
SSR (scale = 15 pixels)	8.4850	2.4007
SSR (scale = 80 pixels)	17.7173	0.6783
SSR (scale = 250 pixels)	27.1259	0.1848
MSR ( $\omega_1 = 1/3$ , $\omega_2 = 1/3$ , $\omega_3 = 1/3$ )	15.0569	1.0086
MSR ( $\omega_1 = 2/4$ , $\omega_2 = 1/4$ , $\omega_3 = 1/4$ )	12.9146	1.3437
MSR ( $\omega_1 = 1/4$ , $\omega_2 = 2/4$ , $\omega_3 = 1/4$ )	15.6836	0.9224
MSR ( $\omega_1 = 1/4$ , $\omega_2 = 1/4$ , $\omega_3 = 2/4$ )	17.0583	0.7798
MSR ( $\omega_1 = 3/5$ , $\omega_2 = 1/5$ , $\omega_3 = 1/5$ )	11.8356	1.5544
MSR ( $\omega_1 = 4/6$ , $\omega_2 = 1/6$ , $\omega_3 = 1/6$ )	11.1821	1.6973
SSR (scale = 10 pixels)	7.7921	2.6780
SSR (scale = 50 pixels)	14.1465	1.0492
SSR (scale = 60 pixels)	14.6290	1.0056
SSR (scale = 120 pixels)	22.4192	0.3782
SSR (scale = 200 pixels)	26.5111	0.2121
SSR (scale = 220 pixels)	26.8245	0.1987
MSR <sub>2</sub> ( $\omega_1 = 1/3$ , $\omega_2 = 1/3$ , $\omega_3 = 1/3$ )	13.7010	1.2132
MSR <sub>2</sub> ( $\omega_1 = 2/4$ , $\omega_2 = 1/4$ , $\omega_3 = 1/4$ )	11.8239	1.5718
MSR <sub>2</sub> ( $\omega_1 = 3/5$ , $\omega_2 = 1/5$ , $\omega_3 = 1/5$ )	10.8591	1.7957
Histogram equalization	7.7978	1.5199
Local histogram equalization	7.4683	1.5236
Wavelet-based algorithm	6.0785	1.1225

**TABLE 1:** Comparisons of PSNR and CNR for phantom images obtained from retinex algorithms with those obtained from histogram equalization, local histogram equalization, and the wavelet-based algorithm.

Algorithm	PSNR (dB)	CNR
SSR (scale = 15 pixels)	7.5729	3.8213
SSR (scale = 80 pixels)	16.7675	0.9751
SSR (scale = 250 pixels)	21.3775	0.3568
MSR ( $\omega_1 = 1/3$ , $\omega_2 = 1/3$ , $\omega_3 = 1/3$ )	13.8641	1.5566
MSR ( $\omega_1 = 2/4$ , $\omega_2 = 1/4$ , $\omega_3 = 1/4$ )	11.8648	2.0922
MSR ( $\omega_1 = 1/4$ , $\omega_2 = 2/4$ , $\omega_3 = 1/4$ )	14.5375	1.4031

MSR ( $\omega_1 = 1/4, \omega_2 = 1/4, \omega_3 = 2/4$ )	15.5348	1.2157
MSR ( $\omega_1 = 1/5, \omega_2 = 3/5, \omega_3 = 1/5$ )	14.9590	1.3135
SSR (scale = 10 pixels)	7.0382	4.2851
SSR (scale = 60 pixels)	13.6414	1.5104
SSR (scale = 220 pixels)	21.2816	0.3752
MSR <sub>2</sub> ( $\omega_1 = 1/3, \omega_2 = 1/3, \omega_3 = 1/3$ )	12.6385	1.8747
MSR <sub>2</sub> ( $\omega_1 = 1/4, \omega_2 = 2/4, \omega_3 = 1/4$ )	12.8957	1.7817
MSR <sub>2</sub> ( $\omega_1 = 1/4, \omega_2 = 1/4, \omega_3 = 2/4$ )	14.4219	1.4399
MSR <sub>2</sub> ( $\omega_1 = 2/6, \omega_2 = 3/6, \omega_3 = 1/6$ )	11.7580	2.1157
Histogram equalization	6.4478	1.8631
Local histogram equalization	6.3042	1.8807
Wavelet-based algorithm	11.8304	0.8571

**TABLE 2:** Comparisons of PSNR and CNR for animal images obtained from retinex algorithms with those obtained from histogram equalization, local histogram equalization, and the wavelet-based algorithm.

#### 4. DISCUSSION

The inhomogeneity and anatomic-structure blurring found in images captured by surface receiving coils was due to variations in image brightness. The inhomogeneities of MR images were very low frequency components in frequency domain of images. The retinex algorithm [33, 34] especially performed to remove the very low frequency components of images by an estimator constructed with a similar lowpass filter from a Gaussian surround function as described in Eq. (11) for the purpose of correction of the inhomogeneous MR images. The variations of inhomogeneity in MR images received with surface coils were shown in Fig. 2(a) and Fig. 3(a). Hence, MR postprocessing techniques were crucial in improving the structural details and homogeneity of such brain images. In the present study, we proposed an easy, low-cost software-based method to solve these problems, also avoiding expensive charges to the imaging hardware. Our novel retinex algorithm successfully corrected a nonuniform grayscale, enhanced contrast, corrected inhomogeneity, and clarified the MFB and MT areas in deep brain structures of MR images captured by surface coils (see Fig. 3).

For evaluating the performance of correction of inhomogeneous MR images, the two indices, PSNR and CNR [9, 37, 38], were proposed to compare the performance of correction of inhomogeneous MR images using retinex algorithm with other correction algorithms. The retinex algorithm improved the quality of phantom images in terms of visual rendition and dynamic range compression, with reduced errors and noise, and correspondingly higher PSNR and CNR values. Similar results were found for animal images, except that PSNR increased whereas CNR decreased. (see Table 1 and Table 2) This may indicate that retinex processing of animal data should combine with appropriate reference objects.

For comparison, consider the approach proposed by Jobson et al [33, 34]. The MR images obtained with the retinex algorithm were also better than those obtained with histogram equalization, local histogram equalization, and the wavelet-based algorithm, in terms of dynamic-range compression, brightness constancy, and overall visual rendition. The PSNR and CNR values were also higher for retinex than for the other correction algorithms. Furthermore, the advantages of the retinex were that the weightings of MSR and scales of SSR could be modulated to improve image correction and contrast enhancement performance. The retinex algorithm could also be used to increase the SNR and dynamic-range compression in other types of medical image, such as those captured by computed tomography, digital X-ray systems, and digital mammography.

## ACKNOWLEDGMENTS

This work was supported by grant NSC95-2221-E-009-171-MY3 from the National Science Council, Taiwan, ROC. The authors acknowledge the technical support from the Functional and Micro-Magnetic Resonance Imaging Center, which is funded by the National Research Program for Genomic Medicine, National Science Council, Taiwan, ROC, under grant NSC93-3112-B-001-006-Y. Furthermore, the authors thank Dr. Chi-Hsien Chen for his assistance with and valuable comments on MR image analysis, and for many helpful discussions on wavelet-based algorithms.

## REFERENCES

1. B. R. Conway, M. S. Livingstone. "Spatial and temporal properties of cone signals in alert macaque primary visual cortex". J Neuroscience, 26(42):10826–10846 2006
2. Z. Cho, J. P. Jones and M. Singh. "Foundations of medical imaging", New York: JohnWiley and Sons, (1993)
3. B. R. Conway. "Spatial structure of cone inputs to color cells in alert macaque primary visual cortex". J Neuroscience, 21:2768–2783 2001
4. H. S. Zadeh, J. P. Windham, D. J. Peck, A. E. Yagle "A comparative analysis of several transforms for enhancement and segmentation of magnetic resonance image scene sequences" IEEE Trans Med Imag, 11:302–318 1992
5. E. B. Boskamp. "Improved surface coil imaging in MR: decoupling of the excitation and receiver coils". Radiology, 157(2):449–452, 1985
6. M. L. Wood, M. J. Shivji and P. L. Stanchev. "Planar motion correction with use of k-space data acquired in Fourier MR imaging". J Magn Reson Imaging, 5(1):57–64, 1995
7. R. A. Zoroofi, Y. Sato, S. Tamura, H. Naito and L. Tang. "An improved L method for MRI artifact correction due to translational motion in the imaging plane". IEEE Trans Med Imag, 14:471–479, 1995
8. J. G. Sled, A. P. Zijdenbos and AC Evans. "A nonparametric method for automatic correction of intensity nonuniformity in MRI data". IEEE Trans Med Imag, 17(1):87–97, 1998
9. C. B. Ahn, Y. C. Song and D. J. Park. "Adaptive template filtering for signal-to-noise ratio enhancement in magnetic resonance imaging". IEEE Trans Med Imag, 18(6):549–556, 1999.
10. M. Styner, C. Brechbuhler, G. Szekeley, and G. Gerig. "Parametric estimate of intensity inhomogeneities applied to MRI". IEEE Trans Med Imag,; 19(3):153–165, 2000
11. B. Likar, M. A. Viergever and F. Pernus, "Restrospective correction of MR intensity inhomogeneity by information minimization". IEEE Trans Med Imag, 20:1398–1410, 2001.
12. F. H. Lin, Y. J. Chen, J. W. Belliveau and L. L. Wald. "A wavelet-based approximation of surface coil sensitivity profile for correction of image intensity inhomogeneity and parallel imaging reconstruction". Human Brain Mapp, 19(2):96–111, 2003
13. C. Han, T. S. Hatsukami and C. Yuan. "A multi-scale method for automatic correction of intensity non-uniformity in MR images". J Magn Reson Imaging, 13(3):428–436, 2001
14. Z. Hou. "A review on MR image intensity inhomogeneity correction". International Journal of Biomedical Imaging, pp. 1–11, 2006
15. R. R. Edelman, et al. "Surface coil MR imaging of abdominal viscera. Part 1: theory, technique, and initial results". Radiology, 157(2):425–430, 1985
16. E. A. Vokurka, N. A. Watson, Y. Watson, NA Thacker and A. Jackson "Improved high resolution MR imaging for surface coils using automated intensity non-uniformity correction: feasibility study in the Orbit". J Magn Reson Imaging, 14(5):540–546, 2001
17. R. Ouwerkerk, R. G. Weiss and P. A. Bottomley. "Measuring human cardiac tissue sodium concentrations using surface coils, adiabatic excitation, and twisted projection imaging with minimal  $T_2$  losses". J Magn Reson Imaging, 21(5):546–555, 2005
18. C. M. Collins, W. Liu, J. Wang, R. Gruetter, J. T. Vaughan, K. Ugurbil, M. B. Smith. "Temperature and SAR calculations for a human head within volume and surface coils at 64 and 300 M Hz". J Magn Reson Imaging, 19:650–656, 2004
19. J. Wosik, L. M. Xie, K. Nesteruk, L. Xue, J. A. Bankson and J. D. Hazle. "Superconducting single and phased-array probes for clinical and research MRI". IEEE Trans Appl Supercon, 13(2):1050–1055, 2003

20. R. C. Gonzalez, R. E. Woods. *"Digital image processing"*, 2nd ed., New Jersey: Prentice Hall, Inc., (2002)
21. S. D. Chen, A. R. Ramli. *"Preserving brightness in histogram equalization based contrast enhancement techniques"*. Digit Sig Proc, 14(5):413–428, 2004
22. V Caselles, JL Lisani, JM Morel and G. Sapiro. *"Shape preserving local histogram modification"*. IEEE Trans Imag Proc, 8(2):220–230, 1999
23. H. D. Cheng, X. J. Shi. *"A simple and effective histogram equalization approach to image enhancement"*. Digit Sig Proc, 14(2):158–170, 2004
24. Y. Sun, D. Parker. *"Small vessel enhancement in MRA images using local maximum mean processing"*. IEEE Trans Imag Proc, 10(11):1687–1699, 2001
25. J. Y. Kim, L. S. Kim, S. H. Hwang. *"An advanced contrast enhancement using partially overlapped sub-block histogram equalization"*. IEEE Trans Cir & Sys for Video Tech, 11(4):475–484, 2001
26. J. Tang, E. Peli and S Acton. *"Image enhancement using a contrast measure in compressed domain"*. IEEE Sig Proc Letters, 10(10):289–292, 2003
27. M Eramian, D Mould. *"Histogram equalization using neighborhood metrics"*. Proceedings of the 2nd Canadian Conference on Computer and Robot Vision, pp. 397–404, 2005
28. E. Land. *"An alternative technique for the computation of the designator in the retinex theory of color vision"*. Proc Natl Acad Sci U S A., 83(10):3078–3080, 1986
29. A. Moore, J. Allman, R. M. Goodman. *"A real-time neural system for color constancy"*. IEEE Trans Neural Networks, 2(2):237–247, 1991
30. A. Moore, G. Fox, J. Allman and R. M. Goodman. *"A VLSI neural network for color constancy," in Advances in Neural Information Processing 3*. D. S. Touretzky, R. Lippman and E. S. Mateo, CA: Morgan Kaufmann, pp. 370–376, 1991
31. A. C. Hurlbert, T. Poggio, *"Synthesizing a color algorithm from examples"*. Science, 239(4839):482–485, 1988
32. A. C. Hurlbert. *"The computation of color"*. PhD dissertation, Mass. Inst. Technol., Cambridge, MA, 1989
33. D. J. Jobson, Z. Rahman and G. A. Woodell. *"Properties and performance of a center/surround retinex"*. IEEE Trans Imag Proc, 6(3):451–462, 1997
34. D. J. Jobson, Z. Rahman and G. A. Woodell. *"A multiscale retinex for bridging the gap between color images and the human observation of scenes"*. IEEE Trans Imag Proc, 6(7):965–976, 1997
35. D. E. Bowker, R. E. Davis, D. L. Myrick, K. Stacy and W. L. Jones, *"Spectral reflectances of natural targets for use in remote sensing studies"*. NASA Ref Pub, 1985.
36. D. H. Brainard, B. A. Wandell. *"An analysis of the retinex theory of color vision"*. J Opt Soc Amer A, 3(10):1651–1661, 1986
37. G. W. Wei. *"Generalized perona malik-equation for image restoration"*. IEEE Sig Proc Letters, 6(7):165–167, 1999



COMPUTER SCIENCE JOURNALS SDN BHD  
M-3-19, PLAZA DAMAS  
SRI HARTAMAS  
50480, KUALA LUMPUR  
MALAYSIA